

## ARTICLE OPEN



# Single cell atlas of kidney cancer endothelial cells reveals distinct expression profiles and phenotypes

Yuexin Xu<sup>1</sup>✉, Chris P. Miller<sup>1</sup>, Jun Xue<sup>2,3</sup>, Ying Zheng<sup>2,3</sup>, Edus H. Warren<sup>1,4,5</sup>, Scott S. Tykodi<sup>5,6,8</sup> and Shreeram Akilesh<sup>4,7,8</sup>

© The Author(s) 2024

**BACKGROUND:** Tumor endothelial cells (TECs) represent the primary interface between the tumor microenvironment and circulating immune cells, however their phenotypes are incompletely understood in highly vascularized clear cell renal cell carcinoma (ccRCC).

**METHODS:** We purified tumor and matched normal endothelial cells (NECs) from ccRCC specimens and performed single-cell RNA-sequencing to create a reference-quality atlas available as a searchable web resource for gene expression patterns. We established paired primary TECs and NECs cultures for ex vivo functional testing.

**RESULTS:** TECs from multiple donors shared a common phenotype with increased expression of pathways related to extracellular matrix regulation, cell-cell communication, and insulin-like growth factor signaling. This phenotype was shared with hepatocellular carcinoma associated TECs, suggesting convergent TEC phenotypes between unrelated tumors. Cultured TECs stably maintained a core program of differentially regulated genes which promoted resistance to apoptosis after vascular endothelial growth factor removal and increased adhesiveness to subsets of immune cells including regulatory T-cells.

**CONCLUSIONS:** Our studies demonstrate that TECs have a distinct phenotype that is shared by TECs from different tumor types and stable in ex vivo culture. The distinct adhesive interaction of TECs with immune cells raises the possibility of their modulation to improve immune cell-based therapies for RCC.

*BJC Reports*; <https://doi.org/10.1038/s44276-024-00047-9>

## INTRODUCTION

Clear cell renal cell carcinoma (ccRCC) is the most common malignant tumor of the kidney in adults. The majority of spontaneously arising ccRCC tumors exhibit inactivation of the von Hippel-Lindau tumor suppressor gene, which in turn stabilizes the hypoxia-inducible factor (HIF) signaling pathway [1–5]. Constitutive HIF activity stimulates a pro-angiogenic program, including overexpression of vascular endothelial growth factor (VEGF) [6] and, as a result, ccRCC tumors are highly vascularized. Tyrosine kinase inhibitor (TKI) mediated blockade of angiogenic signaling via targeting of VEGF-receptors remains a cornerstone of medical therapy for patients with these tumors [7, 8].

ccRCC tumors are often immune-infiltrated [9] and responsive to immune checkpoint inhibitors, which are now administered in combination with TKIs as primary systemic therapy for advanced disease [10, 11]. Tumor endothelial cells (TECs) and cell-cell junctions are recognized as the gateway for host immune cells entering the tumor microenvironment. Previous studies of TECs using single-cell RNA-seq (scRNA-seq) in various cancers have revealed significant differences in TEC gene expression and functional phenotypes as compared to their normal endothelial cell (NEC) counterparts [12–15]. Despite the highly vascular nature

of ccRCC, previous analyses of TECs in ccRCC are limited to scRNA-seq performed on the entire tumor mass in which TECs represented only a small fraction of the total input cell number [12–14]. Without specific enrichment for TECs, this limited sampling represents an underpowered analysis of the TEC phenotype [16, 17]. In addition, not all ccRCC studies included comparative analysis to matched NECs. Furthermore, none of the prior analyses of TEC from ccRCC assessed the stability of TEC phenotypes in ex vivo primary culture, their barrier function regulating entry of immune cells into the tumor, and their putative role in shaping the infiltrating immune cell phenotype of the tumor microenvironment [18–20].

Therefore, in this study, we purified TECs and NECs from ccRCC nephrectomy tissues to perform an in-depth characterization of their gene expression patterns and phenotypes. We validated that TECs from ccRCC have a phenotype that is distinct from NECs. We found a congruent expression signature for TECs from ccRCC when compared with those from hepatocellular carcinoma, a disease similarly responsive to anti-angiogenic and immune checkpoint inhibitor therapies. We also revealed that many expression programs of TECs were stable in ex vivo culture. Cultured TECs displayed tolerance to VEGF withdrawal and

<sup>1</sup>Translational Science and Therapeutics Division, Fred Hutchinson Cancer Center, Seattle, WA, USA. <sup>2</sup>Department of Bioengineering, University of Washington, Seattle, WA, USA.

<sup>3</sup>Institute for Stem Cell and Regenerative Medicine, University of Washington, Seattle, WA, USA. <sup>4</sup>Department of Laboratory Medicine and Pathology, University of Washington, Seattle, WA, USA.

<sup>5</sup>Department of Medicine, Division of Hematology and Oncology, University of Washington, Seattle, WA, USA. <sup>6</sup>Clinical Research Division, Fred Hutchinson Cancer Center, Seattle, WA, USA. <sup>7</sup>Kidney Research Institute, University of Washington, Seattle, WA, USA. <sup>8</sup>These authors contributed equally: Scott S. Tykodi, Shreeram Akilesh.

✉email: [yxu2@fredhutch.org](mailto:yxu2@fredhutch.org)

enhanced binding to autologous leukocytes, especially T-cells and monocytes. Our analysis platform can be exploited for further study of therapeutic targeting of TECs across tumor types as well as for insight into immune cell binding interactions with TECs, the first component of the tumor microenvironment encountered by immune cells.

## METHODS

### Study cohort

We collected sets of tumor, normal kidney, and PBMC biospecimens from four treatment naïve patients who underwent partial or full nephrectomy surgery (Table S1). Specimens were collected with informed consent and in deidentified fashion under the University of Washington's Institutional Review Board Study 7768. The tumor histology was confirmed as ccRCC for all four patients on their final pathology report.

### Single-cell RNA-sequencing

Tissue single-cell suspensions were stained by DAPI, 1:20 dilution of PE-labeled Mouse anti-Human CD144, and APC anti-human CD31 (clone WM59, Biolegend, San Diego, CA) and sorted by flow cytometry (FACSAria III, BD biosciences). CD144<sup>+</sup>DAPI<sup>-</sup> ECs and DAPI<sup>-</sup> live cells from each sample were sorted into two separate tubes and labeled by TotalSeq™-C0251 anti-human Hashtag 1 Antibody (HTO-1, Biolegend) and HTO-2 respectively according to manufacturer's protocol. The sorted cells were then combined at 2:1 ratio. 5000 DAPI- HUVEC cells labeled with HTO-3 were spiked into each of the samples. Samples were then loaded at 17,000 cells per lane onto a 10X Genomics Controller (10X Genomics, Pleasanton, CA). scRNA-seq libraries were constructed according to the manufacturer's protocol. Pooled V(D)J, 5' GEX, and HTO libraries were sequenced on a NovaSeq 6000 SP100 flowcell (Illumina, San Diego, CA) to obtain 5000 reads/cell, 20,000 reads/cell, and 5000 reads/cell depth, respectively.

### Primary endothelial cell (EC) culture

EC media were made with EBM-2 base media (Lonza, Basel, Switzerland) with 1% anti-anti (Thermo Fisher Scientific, Waltham, MA) and 10% FBS (ThermoFisher Scientific, Waltham, MA), supplement with 500x ECGS (Cell Biologics, Chicago, IL) and 50ug/mL Heparin (Thermo Fisher Scientific). To enrich ECs, human EpCAM microbeads (Miltenyi Biotec) were used to deplete epithelial cells from single-cell suspensions. The EC cultures were maintained in recombinant human VEGF-165 (PeproTech, Rocky Hill, NJ) at 40 ng/mL and 1% low O<sub>2</sub> condition 8 days. The passage one cultures were purified further by 1:20 dilution of PE-labeled Mouse anti-Human CD144 (clone 55-7H1; BD Biosciences, San Jose, CA) sorting and then culture for two passages with 20 ng/μL human VEGF containing EC media at the same low O<sub>2</sub> condition.

For VEGF retrieval experiments, normal adjacent tissue (NAT) and tumor derived ECs were stained by CellTracker™ Red CMTPX Dye (Thermo Fisher Scientific) at 37 degrees for 30 min, then maintained in the presence or absence of 20 ng/mL VEGF-containing media. Two days after the culture, the floating cells were harvested, and the plates were imaged. The remaining adherent cells were harvested and combined with the floating cells. Overall viability was assessed by DAPI staining by flow cytometry. The % confluency was measured by Fiji ImageJ [21] on the image stacks by applying macro functions first identify the cell boarder and then measure the % of area within the cell boarder on each frame.

### RNA in situ hybridization (RNA-ISH)

5 μm FFPE sections of RCC tumor and matched NAT from the 4 donors used for scRNA-seq were used for RNA-ISH using ACDBio's primary probes targeting *IGFBP3* (Catalog # 310351, ACDBio, Newark, CA) and *IGFBP5* (Catalog # 452381, ACDBio) and the RNAScope 2.5 HD-RED development kit (Catalog # 322350, ACDBio). After colorimetric development, slides were cover-slipped with EcoMount (BioCare Medical, Pacheco, CA) and imaged on an Olympus BX41 upright microscope (Tokyo, Japan) equipped with a Leica DFC420 camera (Leica, Wetzlar, Germany).

### Bioinformatics and statistics

The 10X Chromium scRNA-seq outputs were de-multiplexed, mapped to the human reference genome (hg19, GRCh38) and aggregated into one single-cell object through the Cell Ranger V4.0 bioinformatics pipeline (10X Genomics). Batch effect corrections were performed as described [22].

Dimension reduction and clustering of 10X scRNA-seq data were conducted using the Seurat package [23]. The pseudotime analyses were conducted through the Monocle3 package [24–26]. The cell classification was performed by the Garnett R package [27] based on marker genes (Table S2). DEGs were identified using the nonparametric Wilcoxon rank sum test by FindMarkers function of Seurat package to find DEGs from each identity cluster against the remaining cells, with  $\text{min.pct} = 0.25$ ,  $\text{logfc.threshold} = 0.25$ . We used default options for the analysis if not specified otherwise. DEG results were visualized using the EnhancedVolcanoR package (version 1.10.0) <https://github.com/kevinblighe/EnhancedVolcano>. FeaturePlot, DimPlot, and DotPlot functions of the Seurat package were used for visualization of selected genes. The 'VlnPlot' function of the Seurat package was used for violin plots to show the expression level of selected genes with log normalized value by default. Pathway analyses were conducted using the R package clusterProfiler [28].

Raw RNA-seq data were processed by the nextflow nf-core/maseq analysis pipeline using STAR, RSEM, HISAT2 or Salmon with gene/isoform counts and extensive quality control [29]. DEGs were calculated by DEseq2 R package [30]. Pathway analyses were conducted using R package clusterProfiler [28]. Proportional Venn diagram of preserved DEGs was plotted using the BioVenn R package [31].

### Other methods

Other methods are included in the Supplementary Methods.

## RESULTS

### TECs from ccRCC tumors have a gene expression profile distinct from NECs isolated from renal cortex

To characterize the expression phenotype of TECs from ccRCC and compare it to their normal counterpart (NECs) isolated from normal adjacent renal cortex, we performed scRNA-seq on TECs and NECs purified by flow cytometry from four different donor nephrectomies. The four TEC/NEC sample pairs were batched into two separate scRNA-seq libraries. We spiked in human umbilical vein endothelial cells (HUVECs) in all samples to allow us to study batch-to-batch variation between libraries. TECs/NECs, HUVECs and an aliquot of the entire tumor/normal adjacent tissue (NAT) were surface-labeled with unique hashtag oligonucleotide (HTO)-labeled antibodies targeting both human CD298 and  $\beta 2$  microglobulin prior to pooling. The oligonucleotide barcodes attached to the HTO-labeled antibodies remained associated with the cells during library generation. We utilized the readout of these HTO-antibodies as an independent measure of cellular identity at the analysis stage (see below).

Uniform Manifold Approximation and Projection (UMAP) is a nonlinear dimensionality reduction technique to visualize large high-dimensional datasets. Compared to t-distributed Stochastic Neighbor Embedding (tSNE), UMAP has better preservation of the data's global structure and separates groups of similar categories from each other better. UMAP projections showed distinct cell types clustered according to gene expression patterns (Fig. 1a). Using the HTO-barcodes as an orthogonal measure of cell identity, we saw clear separation of isolated ECs (HTO-antibody1) from non-EC cell populations (HTO-antibody2) within tumor/NAT digests and from HUVECs (HTO-antibody3) (Supplementary Fig. 1A–C). In addition, The HTO-antibody3 labeled HUVEC populations showed good overlap between the two libraries indicating minimal batch effect and showing that there was no significant bias in the representation of cells as a function of donor or sequencing library (Supplementary Fig. 1B, D, E). Furthermore, expression of the *ACTB* housekeeping gene was uniform across the different clusters, consistent with comparable transcript counts/sample over the different cell types (Supplementary Fig. 1F). Overall, after quality control and filtering, our dataset consisted of 14,982 total cells (library1: 3630 cells and library2: 11,352 cells), of which, 7512 cells were TECs or NECs (library1: 2467 ECs and library2: 5045 ECs).

Further exploration of the UMAP projection revealed distinct cell type clusters (ECs, immune cells, tumor cells, normal kidney

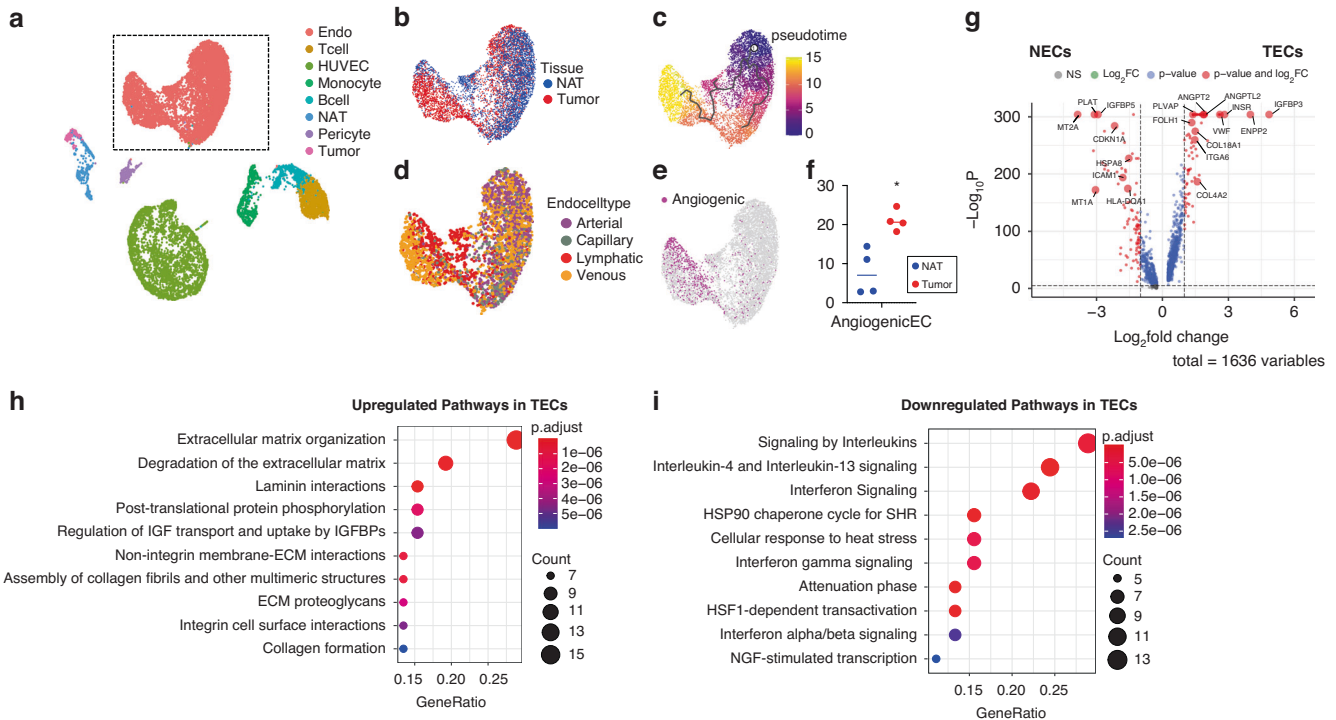


**Fig. 1 Analysis of scRNA-seq transcriptome data for TECs and NECs from ccRCC patients.** **a** UMAP plot of scRNA-seq dataset from 4 subjects colored by clusters. The dashed line marks the EC cluster. UMAP plots marked by **b** tissue origin, **c** pseudotime trajectory, **d** general EC lineages and **(e)** angiogenic ECs. **f** Quantification of angiogenic NECs and TECs numbers. Each dot represents one patient. Statistics:  $*P < 0.05$ ,  $t$ -test. **g** Volcano plot of DEGs in TECs compared with NECs. Dashed lines, cutoffs:  $P < 1 \times 10^{-5}$ ;  $FC = 1$ . **h** Upregulated reactome pathways in TECs with DEGs at  $\log_2FC \geq 1$  compared with NECs. **i** Upregulated reactome pathways in NECs with DEGs at  $\log_2FC \geq 1$  compared with TECs.

epithelial cells, and the control HUVEC clusters, Fig. 1a) that expressed expected lineage markers (Supplementary Fig. 1G), confirming the cell type assignment. For example, ECs expressed *PECAM1* (CD31) and *CDH5* (VE-Cadherin). Though HUVECs expressed EC markers, their overall expression pattern was distinct from primary NECs and TECs. Focused analysis of the primary EC cluster showed a clear separation of TECs and NECs as well as a transitional population with an intermediate phenotype (Fig. 1b). Pseudotime trajectory analysis indicated a phenotypic transition from NECs towards TECs (Fig. 1c). We then classified the ECs according to known phenotypes described as a function of their anatomic location [32] (Table S2). This analysis revealed that NECs from the kidney have a heterogeneous mixture of venous, arterial, capillary, and lymphatic vasculature phenotypes [33–35], whereas TECs predominantly exhibited a venous EC phenotype (Fig. 1d). Cell type classification using a set of angiogenic EC markers (GO angiogenic pathway 0001525 [36, 37]) also revealed that TECs were more likely to exhibit an angiogenic phenotype than NECs (Fig. 1e, f). Taken together, these analyses confirmed that TECs have a phenotype that is distinct from NECs.

To explore the basis of this distinct TEC phenotype, we performed differentially expressed gene (DEG) analysis. A total of 1636 genes were differentially expressed when comparing TECs with NECs (Table S3). The top 3 DEGs highly expressed in TECs versus NECs were *IGFBP3*, *ENPP2*, and *INSR*, whereas *MT2A*, *PLAT*, and *IGFBP5* were the top 3 genes preferentially expressed in NECs (Fig. 1g). Pathway analysis of the DEGs identified extracellular matrix (ECM) organization, laminin interactions, collagen fibrils assembly, non-integrin membrane-ECM interactions, integrin cell surface interactions and IGF regulation as functional pathways upregulated in TECs (Fig. 1h). Exploration of individual matrix metalloproteinase (MMP) and a disintegrin and metalloproteinase with thrombospondin motifs (ADAMTS) family members also

identified several genes with increased expression in TECs (Supplementary Fig. 2A, B). These included enzymes with known roles in promoting angiogenesis such as *MMP9* [38], *MMP14* [39], and *ADAMTS13* [40]. Conversely, in comparison to NECs, TECs had reduced expression of pathways involved in immune regulation such as signaling by interleukins and interferon gamma (Fig. 1i). Importantly, ECs can mediate antigen presentation to T cells as the gateway to the tumor microenvironment by expressing major histocompatibility complex (MHC) class I and II molecules [41]. We therefore examined the expression of MHC I and II molecules in TECs and NECs. MHC molecules were expressed in at least 50% of TECs and NECs with generally lower expression in TECs (Supplementary Fig. 3A). The primary TECs downregulated most of their MHC molecules compared to NECs, except for *HLA-DPA1* and *HLA-DQB1* (Supplementary Fig. 3A). This result is consistent with previous findings in lung cancer that TECs down-regulate MHC class I and II molecules with a negative impact on T cell priming [42].

#### Identification of *IGFBP3* as a marker gene for TECs

UMAP projections clearly showed preferential expression of the top 3 DEGs in TECs (*IGFBP3*, *ENPP2*, and *INSR*) and NECs (*IGFBP5*, *PLAT*, and *MT2A*) (Fig. 2a). Previous studies have proposed *IGFBP3*, *ACKR1*, and *PLVAP* as universal TEC marker genes [15]. While *IGFBP3* was clearly expressed in TECs, we found that *ACKR1* was instead expressed in a transitional subpopulation of ECs derived mainly from normal kidney tissue with a smaller contribution of ECs isolated from the tumor. *PLVAP* had higher expression in TECs, but NECs also expressed this gene and therefore it did not appear to be a TEC-specific marker. The cell-adhesion molecule *VCAM1* has reported expression on a subset of pancreatic TECs [43], though in our dataset, it was localized to the same transitional subpopulation of ECs that expressed *ACKR1*. These UMAP findings

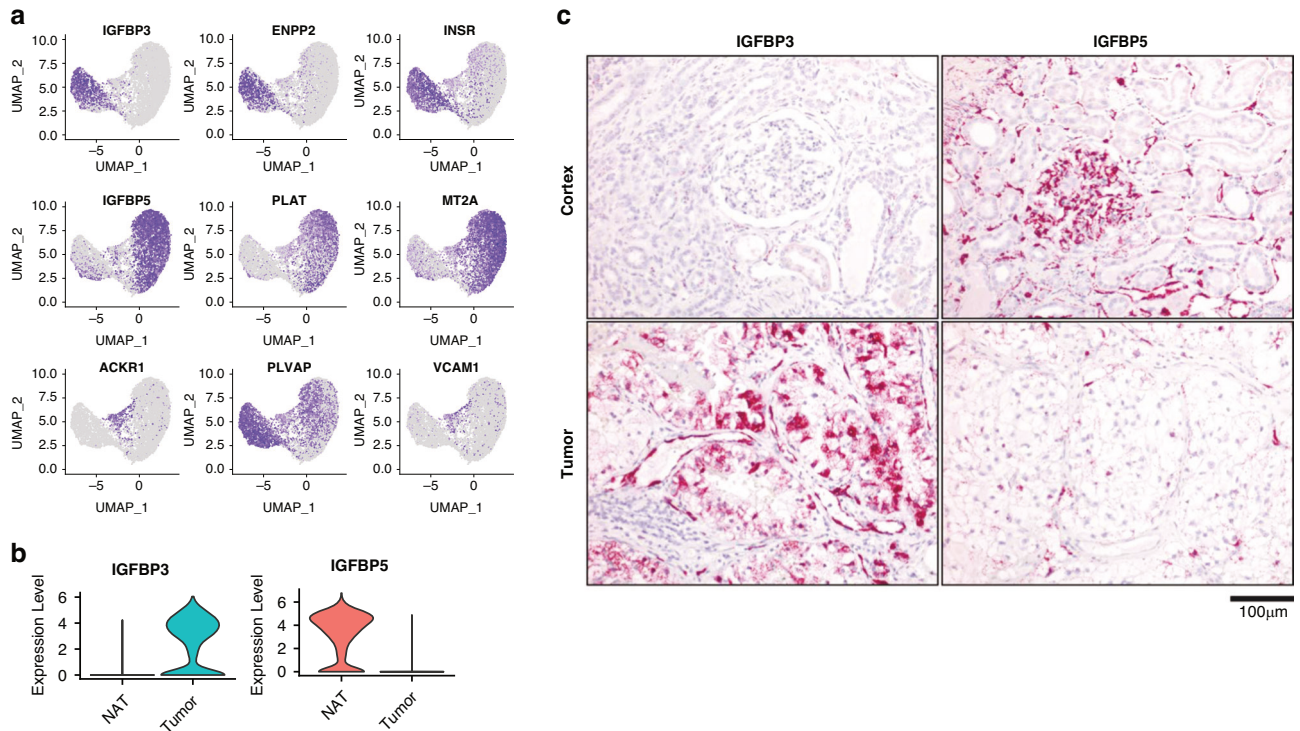


**Fig. 2** *IGFBP3* and *IGFBP5* expression in TECs and NECs. **a** The top three DEGs in TEC, NEC and transitional EC clusters. **b** Single-cell expression of *IGFBP3* and *IGFBP5* in TECs and NECs. **c** RNA-ISH distribution of *IGFBP3* and *IGFBP5* in tumor and normal kidney tissue.

confirmed the results of the DEG analysis but also identified differences from previous studies, which could be due to the increased resolution of our enriched EC dataset and ccRCC-specific patterns.

Given the consistency of *IGFBP3* as a specific marker of TECs in our dataset and in previous studies [15], we validated its anatomic localization as well as that of its paralog *IGFBP5*. Since the IGFbps are primarily secreted to bind with IGFs in the circulation [44] and/or extracellular matrix proteins [45], no *IGFBP3* and *IGFBP5* immunohistochemistry antibodies have been validated so far. Therefore, we used RNA *in situ* hybridization (RNA-ISH) to investigate their anatomic localization on formalin-fixed paraffin-embedded (FFPE) sections of RCC and NAT tissues from the 4 donors. *IGFBP3* and *IGFBP5* were two of the highest DEGs between TECs and NECs (Fig. 2b, Table S3). Correlating with the scRNA-seq data, RNA-ISH for *IGFBP3* showed weak expression in rare peritubular capillaries and some tubules, whereas it showed strong expression in the RCC vasculature and patchy expression in the tumor cells themselves (Fig. 2c). By contrast, *IGFBP5* showed strong staining in glomerular and peritubular capillary ECs in normal kidney tissues as well as some arterial smooth muscle cells (*not shown*). *IGFBP5* showed only minimal and patchy expression in RCC tissues. When we examined all the cell populations in our dataset, we confirmed minimal *IGFBP3* expression in RCC tumor cells as well as *IGFBP5* expression in pericytes, which have an overlapping gene expression signature with arterial smooth muscle cells (Supplementary Fig. 4A–C). Interestingly, HUVECs were discordant with both TEC and NEC phenotypes demonstrating low levels of both *IGFBP3* and *IGFBP5* expression. Having validated *IGFBP3* and *IGFBP5* as markers of RCC-associated TECs and NECs, respectively, we examined the expression profiles of these genes in tumor and normal tissues in The Cancer Genome Atlas (TCGA) dataset. Consistent with our data, *IGFBP3* showed the highest expression in RCC tumors, whereas one of the highest sites of *IGFBP5* expression was normal kidney (Supplementary Fig. 4D, E). Increased expression of *IGFBP3* in RCC (and also in lung

and colorectal cancer) was associated with inferior overall survival, while *IGFBP5* expression had no apparent impact on prognosis in RCC (Supplementary Fig. 4F, G).

#### Integration of published RCC scRNA-seq data highlights the advantage of EC enrichment

Next, we compared the expression data from this study with previously published scRNA-seq datasets generated from ccRCC. We identified 10 published studies with ccRCC scRNA-seq data, of which only 5 included cells likely to be ECs that were defined by measurable coexpression of *PECAM1* and *CDH5*. None of the prior studies specifically enriched for ECs, resulting in an average of 217 ECs/sample (range 2–518/cells sample, Table S4). By contrast, the EC count/sample in this study was 3.7-fold higher than the average published dataset at 939 cells/sample, thus representing the deepest reference dataset for ccRCC ECs. Of the 5 published studies with EC expression data, 2 did not include paired NAT along with the RCC samples (GSE152938 and GSE171306), and study GSE139555 had only 2 ECs per sample on average. The remaining two published datasets from Li et al. (10.17632) [46] and Zhang et al. (GSE159115) [12] included paired TECs and NECs and had adequate EC sampling (207 and 245 cells/sample respectively). We, therefore, co-clustered these two datasets together with our data to generate a unified UMAP projection (Fig. 3a). Reassuringly, 98.4% of ECs from our samples mapped to cell clusters shared with the published datasets (hashed outline). By contrast, only 66.0% of cells from the 2 published studies could be assigned to the composite cell cluster. The non-overlapping cells showed distinct UMAP localizations even between the two published studies, which may be due to methodologic differences, pre-analytic variation, and/or batch effects. Focusing on the shared cluster of ECs across all 3 datasets, we analyzed DEGs in TECs compared to their matched NECs (Fig. 3b). This identified 505 DEGs that were shared across all 3 datasets. Pathway analyses of this gene list identified significant alterations in ECM organization, neutrophil and platelet degranulation, regulation of IGF transport, and uptake by IGFbps and others

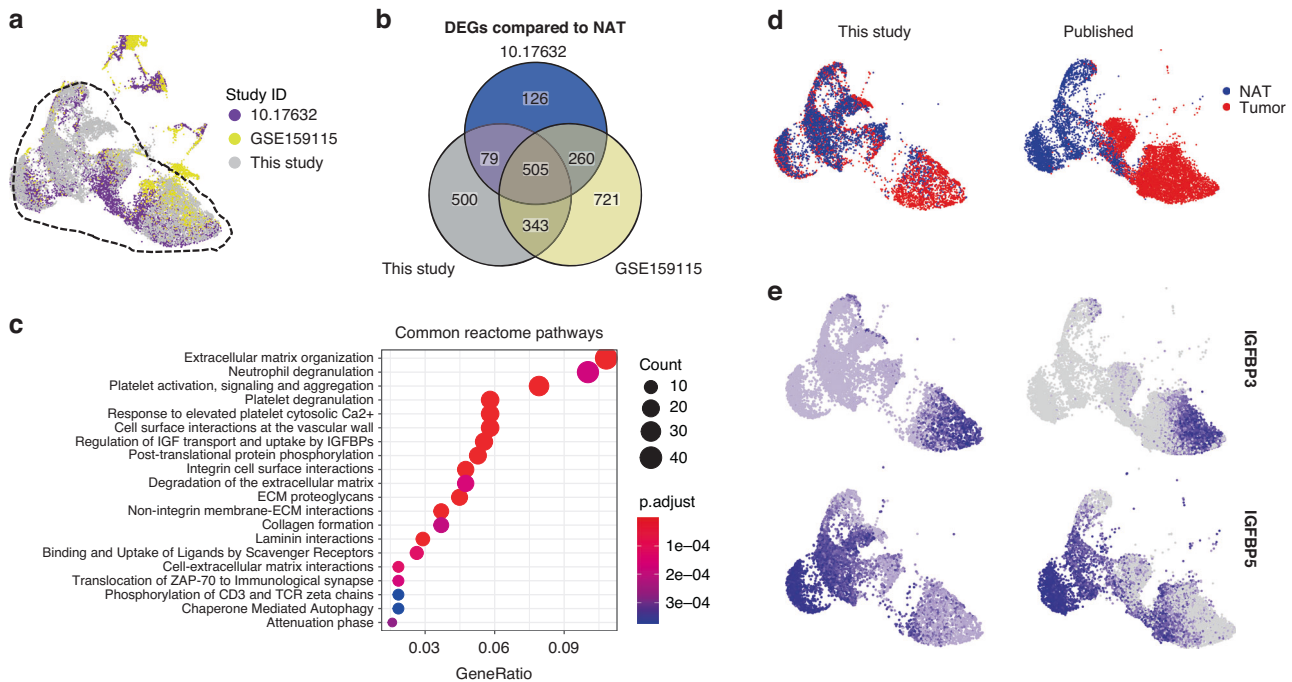


**Fig. 3 Comparison of EC clusters between previously published ccRCC scRNA-seq and this study.** **a** UMAP plot of integrated NEC and TEC populations from ccRCC in previously published studies and this study. The dashed line indicates the cells that are clustered in the common clusters. **b** Overlap between differentially expressed genes (compared to NAT, cutoffs at  $\log_{2}FC = 0.25$ , minimum detection fraction = 0.1) in two previously published studies and this study. **c** Common reactome pathways that are derived from the overlapped DEGs in TECs. **d** UMAP plot colored by tissue origin of previously published datasets and this dataset. **e** *IGFBP3* and *IGFBP5* expression in TECs and NECs.

(Fig. 3c). Assignment of TECs and NECs to the shared UMAP projection showed representation of almost all EC clusters identified in our samples and in the published studies, though there were some minor differences in represented cell populations (Fig. 3d). Of note, the reciprocal expression of *IGFBP3* and *IGFBP5* in TECs and NECs was reproduced in the combined data (Fig. 3e). This analysis demonstrates that the data from our samples recapitulate major EC clusters seen in previous RCC studies, but also provide a much deeper profiling of matched TEC and NEC expression signatures. The advantage of deeper profiling of isolated ECs is evident since *IGFBP5* was not identified as a marker of NEC in either of the two previous studies and *IGFBP3* was not identified as a TEC marker in one of them [12, 46].

### Congruence of TEC phenotypes between kidney and liver cancer

It is not clear if TECs from different types of tumors adopt a unique organ-specific phenotype or a common phenotype that is necessary for tumor growth regardless of tumor location. The second possibility is intriguing since it could lead to therapeutic strategies that target TECs across different tumor types. Supporting this concept, a recent study suggested that tip cells from TECs across different tumor types adopt a congruent phenotype [47]. The deep profiling of ECs enabled by our dataset allowed us to ask a similar question by comparing ccRCC TECs to those from a recently published study on hepatocellular carcinoma (HCC) [20]. We selected this dataset for comparison with ours based on the following criteria: (1) the HCC dataset was collected on both tumor-associated ECs and paired normal tissue-associated ECs isolated from primary tissues, (2) the dataset was generated from samples that were treatment naïve, (3) the dataset was annotated in detail to include the metadata files that allowed for full understanding of the sample and cell population attributes as well cellular subsets, (4) the dataset included a similar EC cell number as our study which allowed for proper meta-analysis, and (5) the dataset was freely available and its structure could be compared with our own data using the Seurat

R package to anchor the common genes. As we did previously for the RCC scRNA-seq datasets, we combined the scRNA-seq data from hepatocellular carcinoma with our own data to create a unified UMAP projection (Fig. 4a). 92.4% of our RCC TECs overlapped with the HCC TECs and conversely, 75.8% of TECs from the HCC dataset overlapped with TEC clusters also present in this RCC study. While there were TEC populations that were unique to both cancer types, this analysis confirmed that the majority of TECs from both kidney and liver tumors were clustered together and exhibited a congruent expression phenotype (Fig. 4a). By contrast, only 37.3% of NECs from normal kidney overlapped with NEC clusters in liver and reciprocally, 51.7% of NECs from normal liver overlapped with NEC clusters in kidney. This finding suggested that normal tissues have NECs with distinct and organ-specific phenotypes. We then asked which genes were differentially expressed between TECs and NECs in both liver and kidney cancer (Fig. 4b). 561 DEGs were shared between both cancer types and these genes were enriched for many of the same pathways previously seen in RCC TECs alone (Fig. 4c). Mapping onto the combined UMAP projection identified unique NEC and TEC populations in both tissues (Fig. 4d). *IGFBP3* expression remained a marker of both kidney cancer and liver TECs, however, *IGFBP5* expression was mainly seen in the kidney and not in liver NECs (Fig. 4e). These analyses showed that while NECs from different organs retained distinct phenotypes that may be important for each organ's unique functions, by contrast, the majority of TECs from two different tumor types shared a congruent gene expression profile with upregulated pathways related to ECM organization, neutrophil/platelet degranulation, IGF transport and uptake by IGFs, and others.

### TECs and NECs maintain their distinct gene expression patterns in ex vivo cell culture

A prerequisite to understanding the functional properties of unique cell types is to establish an in vitro culture system. Few previous studies of TECs have examined their properties in vitro, due to their slow growth and poor viability in culture. Using

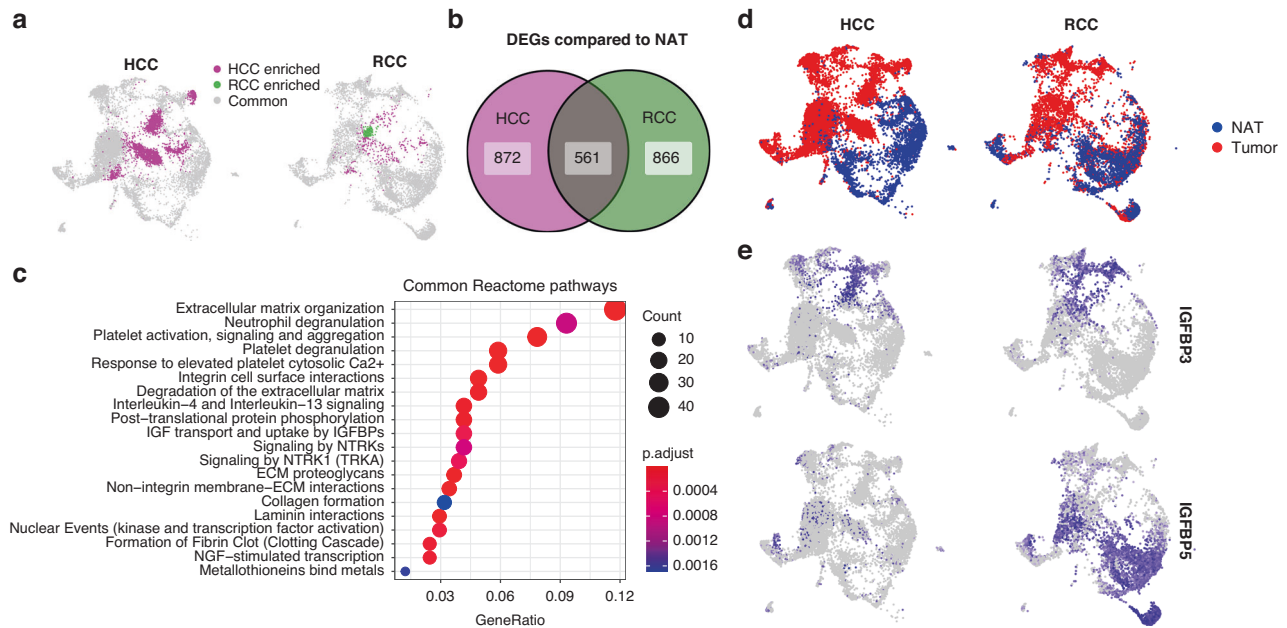


**Fig. 4 Comparison of EC clusters between the previously published HCC scRNA-seq data and RCC data from this study. a** UMAP plot of integrated TEC populations from HCC and RCC. **b** DEG (TECs compared to NECs, cutoffs at  $\log_{2}FC = 0.25$ , minimum detection fraction = 0.1) overlap in the HCC studies and this RCC study. **c** Common reactome pathways that are derived from the overlapping DEGs. **d** UMAP plot colored by tissue origin of ECs from HCC and RCC. **e** *IGFBP3* and *IGFBP5* expression in HCC and RCC.

protocols that we have previously developed, we were able to isolate primary NECs and TECs from 5 donors for successful in vitro culture for up to 2–3 passages in human VEGF-containing media [34, 48]. TECs were larger, stellate, and adopted a lightly overlapping cobblestoned growth pattern in vitro while NECs were smaller, spindle shaped, and adopted a whorled arrangement in culture (Fig. 5a). We then generated bulk RNA-seq data from ECs at passage 3 as well as primary TECs and NECs freshly isolated (not cultured) from the same donors. We detected 1002 DEGs between cultured TECs and NECs compared to 3028 DEGs between primary isolated TECs and NECs. Comparison of the overlap of the DEGs between TECs and NECs showed that, although culturing ECs in vitro reduced the overall number of DEGs, 783 (78.1%) of cultured EC DEGs were still shared with the primary purified ECs (Fig. 5b). Cultured endothelial cell lines derived from tumor and normal kidney both downregulated MHC levels compared to their primary isolated counterparts (Supplementary Fig. 3B). This result is consistent with previous reports on HUVEC cells [49]. This may be due to the absence of the immune microenvironment in ex vivo culture and the lack of cytokines such as  $IFN-\gamma$  that stimulate the expression of MHC [50, 51] via IFN-regulatory factors (IRFs) [52] and IFN-sensitive response element (ISRE) motifs in the MHC promoter region [53]. Early attempts at culturing human ECs demonstrated that co-culture with activated T cells [49], or the addition of  $IFN-\gamma$  indeed boosted MHC levels on HUVEC cells in vitro [54].

To explore the core programs retained by TECs and NECs in culture, we performed pathway enrichment analysis of the shared DEGs. The major upregulated pathways that were conserved in vitro related to neutrophil degranulation, ECM organization, and regulation of interactions with immune/lymphoid cells (Fig. 5c). The major downregulated pathways preserved in TECs in vitro related to GPCR ligand binding, ERBB4 and ERBB2 signaling (Fig. 5d). Next, using quantitative RT-PCR (Table S5), we validated our RNA-seq findings using key TEC and NEC marker genes previously identified (Fig. 5e). The differentially expressed genes *PLVAP*, *ENPP2* also showed the expected pattern of expression in the Protein Atlas IHC database ([www.proteinatlas.org](http://www.proteinatlas.org)), thereby

validating the results of our study. These experiments demonstrated that primary cultures of TECs and NECs could be established in vitro and retain key expression programs of their freshly isolated counterparts.

#### TECs are resistant to VEGF withdrawal and exhibit distinct binding preferences for $CD45^{+}$ leukocytes

Having established conditions for primary culture of TECs and NECs, we next explored their phenotypic and functional differences in vitro. Previous studies demonstrated that the survival of NECs from kidney in culture requires supplementation with VEGF in the culture medium [55]. We first assessed whether TECs and NECs exhibited differential sensitivity to this important trophic factor by removing it from the culture. Within 48 h of VEGF removal, NECs from 4 donors showed a sharp reduction in viability as assessed by DAPI flow staining (Fig. 6a). In contrast, TECs from those same 4 donors showed no loss in viability under the same conditions of VEGF withdrawal. We also performed live cell imaging of TECs and NECs over 48 h (Fig. 6b). TECs showed a comparable increase in percent confluency over the 48-h assay period with or without the presence of VEGF in the culture medium. In contrast, the percent confluency of NECs increased much more slowly without VEGF compared to the presence of VEGF. This differential sensitivity of TECs and NECs to VEGF may be related to the higher expression of KDR and other receptors for autocrine or serum-derived trophic factors both in the isolated and ex vivo cultured ECs (Supplementary Fig. 5).

TECs represent the first barrier to entry of immune cells into the tumor mass and are an integral component of the tumor microenvironment. Immune regulatory pathways were altered in our analysis of DEGs both in freshly isolated (Fig. 1) and cultured TECs (Fig. 5). This observation led us to test whether  $CD45^{+}$  leukocytes exhibited different adherence to TECs versus NECs. We isolated  $CD45^{+}$  leukocytes from the tumor mass, NAT, or peripheral blood mononuclear cells (PBMCs). We applied fluorescently labeled leukocytes to autologous labeled TECs or NECs and studied their interaction in the InCuCyte imaging platform (Fig. 6c). After 24 h of co-culture, we enumerated bound  $CD45^{+}$  leukocytes and

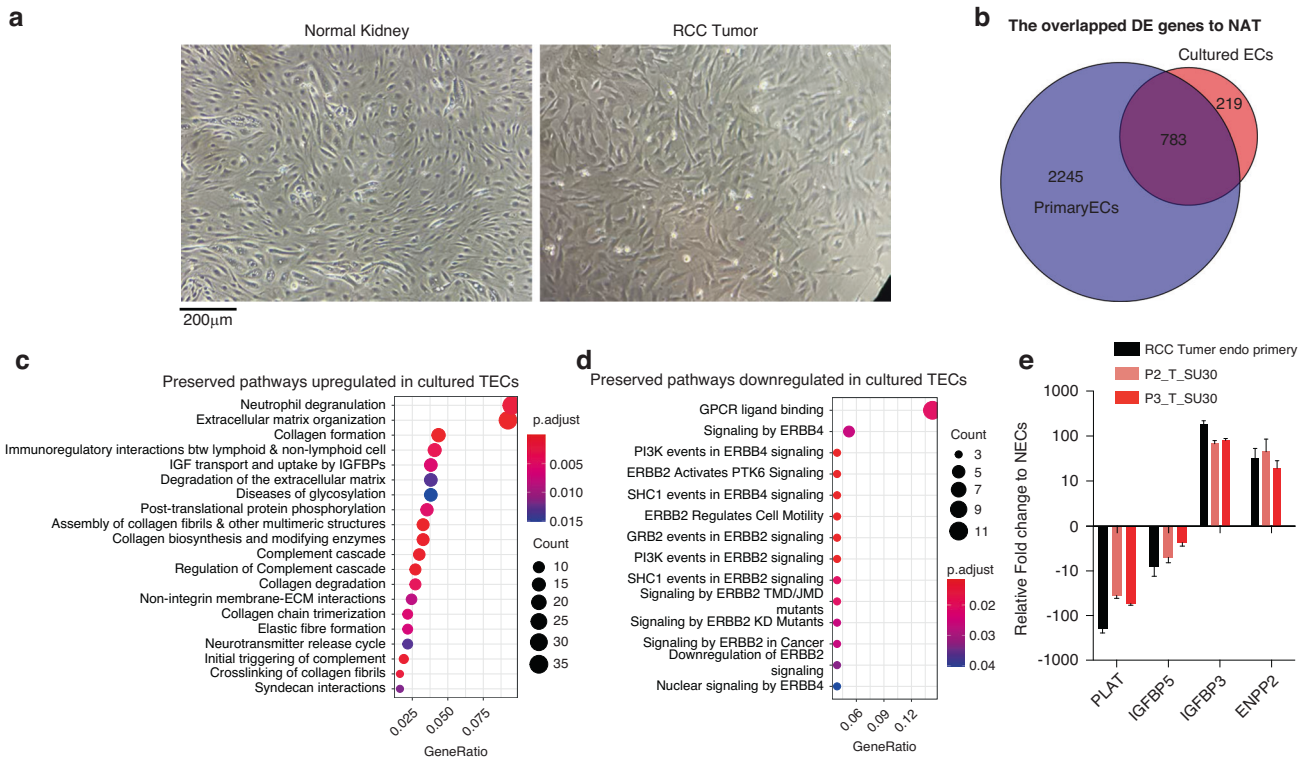


**Fig. 5 Phenotype and gene expression of in vitro cultured TECs and NECs.** **a** Cell morphology of cultured TECs and NECs at passage 3 in a 10X brightfield microscope. **b** Venn diagram of DEGs ( $p_{adj} < 0.05$ ) in TECs compared with NECs and the overlap between cultured and primary ECs. **c, d** Preserved pathways in cultured TECs derived from overlapping differentially expressed genes that are upregulated ( $\log_2FC \geq 1$ ) or downregulated ( $\log_2FC \leq -1$ ). **e** Key marker gene expression compared to NECs in the primary, passage 2, and passage 3 cultures.

normalized that count to the number of TECs or NECs in the culture (Fig. 6d). Regardless of their origin (tumor, NAT, PBMC), more CD45<sup>+</sup> leukocytes adhered to TECs compared to NECs (Fig. 6e). We then used flow cytometry to determine if specific CD45<sup>+</sup> leukocyte subsets were responsible for this difference (Supplementary Fig. 6A). We determined the relative fold binding of specific leukocyte subsets as a function of their origin (Fig. 6f, Supplementary Fig. 6B). Regardless of their tissue of origin, T-cells, and monocytes but not B cells and NK cells were more likely to interact with TECs. Although they were few in number, CD4<sup>+</sup>CD25<sup>+</sup> T regulatory cells were much more likely to adhere to TECs versus NECs. These results may provide an explanation for the preferential recruitment of T-cells and monocytes into the RCC tumor microenvironment that has been reported previously [56]. Taken together, these studies demonstrated the utility of *in vitro* culture of TECs and NECs to study their distinct functional and immunological properties.

## DISCUSSION

TECs are an important component of the tumor microenvironment and represent a contact interface between the circulation and the tumor. Since ECs comprise a small proportion of cells in a tissue, studies without enrichment will be underpowered to detect their heterogeneity. In comparison to the previous ccRCC scRNA-seq studies [12, 46], we provide the deepest characterization of enriched TECs and matched NECs reported to date. This allowed identification of selective *IGFBP3* expression in RCC TECs, as well as altered expression of ECM regulation pathways, which were not detected in prior studies. IGFBPs have dual functions in regulating insulin growth factor (IGF) pathway. They bind to IGFs in circulation to prolong the half-life of IGFs [44] and promote IGF signaling. Conversely, IGFBP isoforms with higher binding affinity

than their cognate IGFs can sequester free IGFs, therefore suppressing IGF signaling [57]. Many IGFBPs exist in these counter-regulatory pairs. It is interesting that IGFBP3 and IGFBP5 are themselves a counter-regulatory pair and their divergent expression patterns in TECs and NECs suggest an important role for IGF signaling in establishing EC phenotypes. *IGFBP* family members show selective expression in various NEC types from kidney [58]. Of these, *IGFBP3* is very focally expressed in peritubular capillary ECs in normal kidney [59], whereas it is broadly expressed in TECs in HCC [15] and ccRCC [15]. One possible mechanism for *IGFBP3* induction in TECs may be the hypoxic tumor microenvironment since it is a HIF-regulated gene [60–62]. *IGFBP3* maintained increased expression in TECs compared to NECs, even when both were cultured under *ex vivo* hypoxic conditions (1% O<sub>2</sub>). *IGFBP3* can promote sprouting angiogenesis [63–65], and retinal neovascularization [66], and the proportion of TECs with an angiogenic phenotype is thought to correlate with susceptibility to anti-VEGF therapy [47]. This correlates with our observations of the relatively high proportion of TECs with an angiogenic phenotype in RCC (Fig. 1), and the negative prognosis of high *IGFBP3* expression in RCC (Supplementary Fig. 2). However, direct targeting of *IGFBP3* as a common TEC-directed therapy may not be straightforward since it appears to have tumor-promoting and anti-tumor effects in different cancers [67]. While it is intriguing that a recent study showed that direct blockade of *IGFBP3* may provide a new therapeutic avenue in RCC [68], this is tempered by lack of efficacy of blockade of *IGFBP3*'s receptor IGF1R in recent clinical trials [69]. In addition, *IGFBP3* may have roles beyond its binding to IGF1R, and therefore further study of its function in RCC TECs is warranted.

Another advance in our study is the description of molecular phenotypes that are retained by TECs and NECs in *ex vivo* culture. We

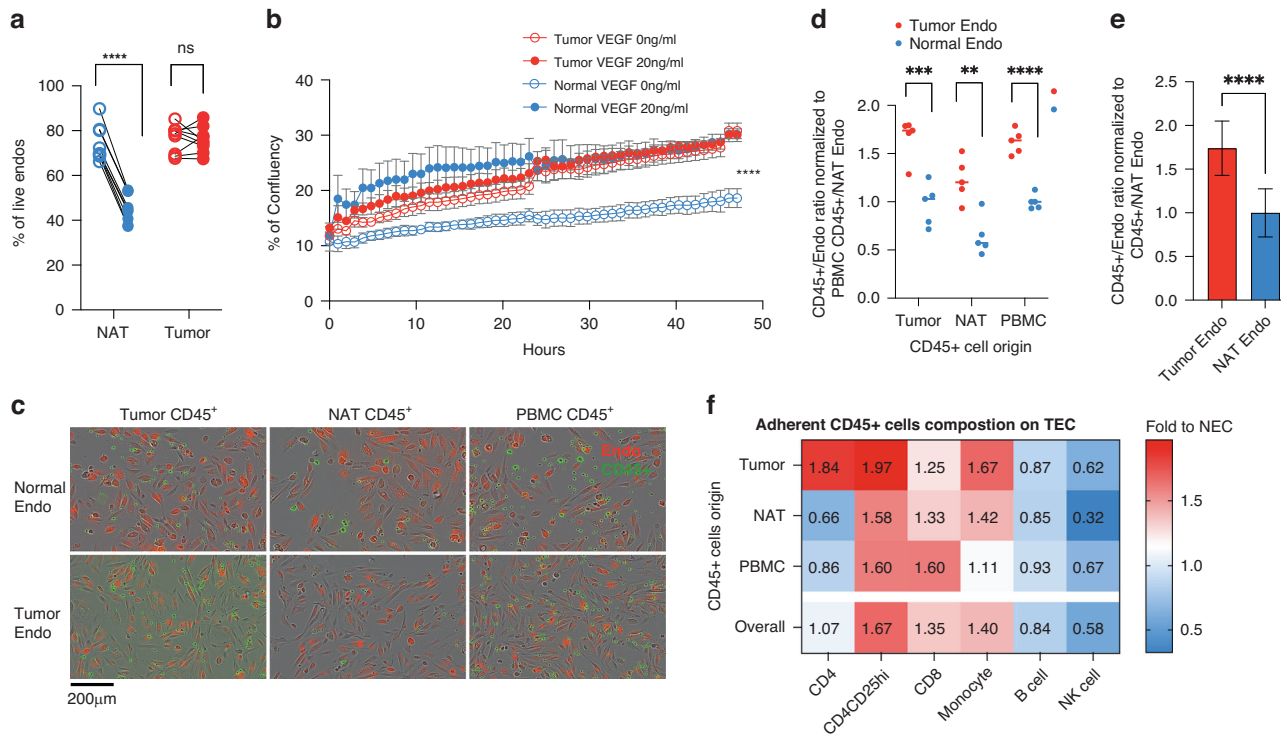


**Fig. 6 Co-culture of immune cells and in vitro established ECs.** **a** The percent of live EC (DAPI- population) after 48 h of VEGF withdrawal. **b** The percent of culture confluency over time. **c** Adherent leukocytes (green) and ECs (red) after 24 h of co-culture. **d** Adherent CD45<sup>+</sup> leukocyte / EC ratio normalized to PBMC CD45<sup>+</sup>/NECs determined by flow cytometry after 24 h of each co-culture combination. **e** Averaged adherent CD45<sup>+</sup> leukocytes from different origins / EC ratio normalized to averaged CD45<sup>+</sup> / NECs. **f** Adherent leukocyte composition on TECs. The percent of total leukocytes of each leukocyte population on TECs were compared to the corresponding % of population on NECs. Fold changes are displayed. Statistics: *t*-test, \*\**P* ≤ 0.01, \*\*\**P* ≤ 0.001, \*\*\*\**P* ≤ 0.0001.

found that TECs were more resistant to cell death after withdrawal of VEGF. This finding is consistent with a previous study that reported proangiogenic properties and resistance of RCC TECs to vincristine-induced apoptosis compared to NECs [70]. Analysis of retained expression signatures showed that TECs had altered expression of pathways regulating the ECM, IGF pathways and immunoregulation in ex vivo culture. We leveraged our ability to study these properties since TECs have been proposed to have multiple immunomodulatory roles in tumors such as anergy induction, antigen presentation, and secretion of factors that affect T-cell migration and priming [71]. Our experiments exploring the interaction of autologous immune cell subsets with ECs demonstrated that CD8<sup>+</sup> T-cells and monocytes increasingly adhere to TECs compared with NECs, which may contribute to the observation that ccRCC tumors often show increased infiltration of T cells and monocytes compared to normal kidney tissue [56, 72]. We also found that CD4<sup>+</sup>CD25<sup>+</sup> cells are able to preferentially adhere to TECs regardless of their tissue of origin (tumor, normal kidney tissue, or peripheral blood). The presence of increased numbers of immunosuppressive CD4<sup>+</sup>CD25<sup>+</sup> regulatory T-cells and exhausted CD8<sup>+</sup> T-cells within RCC tumors explains the efficacy of immune checkpoint inhibitors in overcoming immune tolerance of the tumor [73, 74]. Our results show that the increased frequency of immunosuppressive regulatory T-cells in RCC tumors is likely to be established at the point of T-cell entry into the tumor mass via interactions with TECs. Future studies will explore the interactions of leukocytes with TECs and NECs to assess their penetration into physiologically relevant 3D tumor culture environments [75].

In summary, we investigated a deep reference dataset of isolated and purified TECs from RCC and matched NECs from adjacent kidney tissue. Compared to NECs, TECs had altered expression of genes related to regulation of ECM, IGF signaling and cell-cell interactions, many of which were stably retained in ex vivo primary culture. By comparing EC expression signatures across kidney and

liver cancers, we found that while organ-specific NECs were heterogeneous, the majority of TECs shared a common phenotype. We also demonstrate increased interaction of monocytes and immune suppressive T regulatory cells with TECs providing a mechanism for their enhanced entry into RCC tumors. These findings advance our understanding of TECs in RCC and provide opportunities to exploit or modify their phenotypes as a therapeutic strategy.

#### DATA AVAILABILITY

Sequencing data have been deposited in the National Center for Biotechnology Information Gene Expression Omnibus (scRNA-seq: GSE237425, RNA-seq: GSE237427). Original script is available at [https://github.com/YuexinXu/RCC\\_Endo](https://github.com/YuexinXu/RCC_Endo). The interactive scRNA-seq dataset of RCC and HCC endothelial populations created by Shiny and ShinyCell [76] R packages are available at <https://yxu2.shinyapps.io/shinyapp/>.

#### REFERENCES

- Carmeliet P, Dor Y, Herbert JM, Fukumura D, Brusselmans K, Dewerchin M, et al. Role of HIF-1alpha in hypoxia-mediated apoptosis, cell proliferation and tumour angiogenesis. *Nature*. 1998;394:485–90.
- Gnarra JR, Tory K, Weng Y, Schmidt L, Wei MH, Li H, et al. Mutations of the VHL tumour suppressor gene in renal carcinoma. *Nat Genet*. 1994;7:85–90.
- Iliopoulos O, Levy AP, Jiang C, Kaelin WG Jr, Goldberg MA. Negative regulation of hypoxia-inducible genes by the von Hippel-Lindau protein. *Proc Natl Acad Sci USA*. 1996;93:10595–9.
- Ivan M, Kondo K, Yang H, Kim W, Valiando J, Ohn M, et al. HIF1alpha targeted for VHL-mediated destruction by proline hydroxylation: implications for O2 sensing. *Science*. 2001;292:464–8.
- Jaakkola P, Mole DR, Tian YM, Wilson MI, Gielbert J, Gaskell SJ, et al. Targeting of HIF-alpha to the von Hippel-Lindau ubiquitylation complex by O2-regulated prolyl hydroxylation. *Science*. 2001;292:468–72.



6. Forsythe JA, Jiang BH, Iyer NV, Agani F, Leung SW, Koos RD, et al. Activation of vascular endothelial growth factor gene transcription by hypoxia-inducible factor 1. *Mol Cell Biol*. 1996;16:4604–13.
7. Yang JC, Haworth L, Sherry RM, Hwu P, Schwartzentruber DJ, Topalian SL, et al. A randomized trial of bevacizumab, an anti-vascular endothelial growth factor antibody, for metastatic renal cancer. *N Engl J Med*. 2003;349:427–34.
8. Motzer RJ, Hutson TE, Tomczak P, Michaelson MD, Bukowski RM, Rixe O, et al. Sunitinib versus interferon alfa in metastatic renal-cell carcinoma. *N Engl J Med*. 2007;356:115–24.
9. Senbabaoglu Y, Gejman RS, Winer AG, Liu M, Van Allen EM, de Velasco G, et al. Tumor immune microenvironment characterization in clear cell renal cell carcinoma identifies prognostic and immunotherapeutically relevant messenger RNA signatures. *Genome Biol*. 2016;17:231.
10. Motzer RJ, Penkov K, Haanen J, Rini B, Albiges L, Campbell MT, et al. Avelumab plus axitinib versus sunitinib for advanced renal-cell carcinoma. *N Engl J Med*. 2019;380:1103–15.
11. Rini BI, Plimack ER, Stus V, Gafanov R, Hawkins R, Nosov D, et al. Pembrolizumab plus axitinib versus sunitinib for advanced renal-cell carcinoma. *N Engl J Med*. 2019;380:1116–27.
12. Zhang Y, Narayanan SP, Mannan R, Raskind G, Wang X, Vats P, et al. Single-cell analyses of renal cell cancers reveal insights into tumor microenvironment, cell of origin, and therapy response. *Proc Natl Acad Sci USA*. 2021;118:e2103240118.
13. Alchahin AM, Mei S, Tsea I, Hirz T, Kfoury Y, Dahl D, et al. A transcriptional metastatic signature predicts survival in clear cell renal cell carcinoma. *Nat Commun*. 2022;13:5747.
14. Young MD, Mitchell TJ, Vieira Braga FA, Tran MGB, Stewart BJ, Ferdinand JR, et al. Single-cell transcriptomes from human kidneys reveal the cellular identity of renal tumors. *Science*. 2018;361:594–9.
15. Zeng Q, Mousa M, Nadukkandy AS, Franssens L, Alnaqbi H, Alshamsi FY, et al. Understanding tumour endothelial cell heterogeneity and function from single-cell omics. *Nat Rev Cancer*. 2023;23:544–64.
16. Kalucka J, de Rooij L, Goveia J, Rohlenova K, Dumas SJ, Meta E, et al. Single-cell transcriptome atlas of murine endothelial cells. *Cell*. 2020;180:764–79.e20.
17. Paik DT, Tian L, Williams IM, Rhee S, Zhang H, Liu C, et al. Single-cell RNA sequencing unveils unique transcriptomic signatures of organ-specific endothelial cells. *Circulation*. 2020;142:1848–62.
18. Geldhof V, de Rooij L, Sokol L, Amersfoort J, De Schepper M, Rohlenova K, et al. Single cell atlas identifies lipid-processing and immunomodulatory endothelial cells in healthy and malignant breast. *Nat Commun*. 2022;13:5511.
19. Li Y, Hu X, Lin R, Zhou G, Zhao L, Zhao D, et al. Single-cell landscape reveals active cell subtypes and their interaction in the tumor microenvironment of gastric cancer. *Theranostics*. 2022;12:3818–33.
20. Sharma A, Seow JJW, Dutertre CA, Pai R, Bleriot C, Mishra A, et al. Onco-fetal reprogramming of endothelial cells drives immunosuppressive macrophages in hepatocellular carcinoma. *Cell*. 2020;183:377–94.e21.
21. Schindelin J, Arganda-Carreras I, Frise E, Kaynig V, Longair M, Pietzsch T, et al. Fiji: an open-source platform for biological-image analysis. *Nat Methods*. 2012;9:676–82.
22. Haghverdi L, Lun ATL, Morgan MD, Marioni JC. Batch effects in single-cell RNA-sequencing data are corrected by matching mutual nearest neighbors. *Nat Biotechnol*. 2018;36:421–7.
23. Stuart T, Butler A, Hoffman P, Hafemeister C, Papalexi E, Mauck WM 3rd, et al. Comprehensive integration of single-cell data. *Cell*. 2019;177:1888–902.e21.
24. Trapnell C, Cacchiarelli D, Grimsby J, Pokharel P, Li S, Morse M, et al. The dynamics and regulators of cell fate decisions are revealed by pseudotemporal ordering of single cells. *Nat Biotechnol*. 2014;32:381–6.
25. Qiu X, Mao Q, Tang Y, Wang L, Chawla R, Pliner HA, et al. Reversed graph embedding resolves complex single-cell trajectories. *Nat Methods*. 2017;14:979–82.
26. Cao J, Spielmann M, Qiu X, Huang X, Ibrahim DM, Hill AJ, et al. The single-cell transcriptional landscape of mammalian organogenesis. *Nature*. 2019;566:496–502.
27. Pliner HA, Shendure J, Trapnell C. Supervised classification enables rapid annotation of cell atlases. *Nat Methods*. 2019;16:983–6.
28. Yu G, Wang LG, Han Y, He QY. clusterProfiler: an R package for comparing biological themes among gene clusters. *OMICS*. 2012;16:284–7.
29. Ewels PA, Peltzer A, Fillinger S, Patel H, Alneberg J, Wilm A, et al. The nf-core framework for community-curated bioinformatics pipelines. *Nat Biotechnol*. 2020;38:276–8.
30. Love MI, Huber W, Anders S. Moderated estimation of fold change and dispersion for RNA-seq data with DESeq2. *Genome Biol*. 2014;15:550.
31. Hulsen T, de Vlieg J, Alkema W. BioVenn - a web application for the comparison and visualization of biological lists using area-proportional Venn diagrams. *BMC Genomics*. 2008;9:488.
32. Schupp JC, Adams TS, Cosme C Jr, Raredon MSB, Yuan Y, Omote N, et al. Integrated single-cell atlas of endothelial cells of the human lung. *Circulation*. 2021;144:286–302.
33. Dumas SJ, Meta E, Borri M, Luo Y, Li X, Rabelink TJ, et al. Phenotypic diversity and metabolic specialization of renal endothelial cells. *Nat Rev Nephrol*. 2021;17:441–64.
34. Marcu R, Choi YJ, Xue J, Fortin CL, Wang Y, Nagao RJ, et al. Human organ-specific endothelial cell heterogeneity. *iScience*. 2018;4:20–35.
35. Ribatti D, Ligresti G, Nicosia RF. Kidney endothelial cell heterogeneity, angiocrine activity and paracrine regulatory mechanisms. *Vascul Pharmacol*. 2023;148:107139.
36. Gene Ontology C, Aleksander SA, Balhoff J, Carbon S, Cherry JM, Drabkin JJ, et al. The gene ontology knowledgebase in 2023. *Genetics*. 2023;224:iyad031.
37. Ashburner M, Ball CA, Blake JA, Botstein D, Butler H, Cherry JM. The Gene Ontology Consortium et al. Gene ontology: tool for the unification of biology. *Nat Genet*. 2000;25:25–9.
38. Park JE, Tan HS, Datta A, Lai RC, Zhang H, Meng W, et al. Hypoxic tumor cell modulates its microenvironment to enhance angiogenic and metastatic potential by secretion of proteins and exosomes. *Mol Cell Proteomics*. 2010;9:1085–99.
39. Chang JH, Huang YH, Cunningham CM, Han KY, Chang M, Seiki M, et al. Matrix metalloproteinase 14 modulates signal transduction and angiogenesis in the cornea. *Surv Ophthalmol*. 2016;61:478–97.
40. Lee M, Rodansky ES, Smith JK, Rodgers GM. ADAMTS13 promotes angiogenesis and modulates VEGF-induced angiogenesis. *Microvasc Res*. 2012;84:109–15.
41. Pober JS, Merola J, Liu R, Manes TD. Antigen presentation by vascular cells. *Front Immunol*. 2017;8:1907.
42. Lambrechts D, Wauters E, Boeckx B, Aibar S, Nittner D, Burton O, et al. Phenotype molding of stromal cells in the lung tumor microenvironment. *Nat Med*. 2018;24:1277–89.
43. Shiau C, Su J, Guo JA, Hong TS, Wo JY, Jagadeesh KA, et al. Treatment-associated remodeling of the pancreatic cancer endothelium at single-cell resolution. *Front Oncol*. 2022;12:929950.
44. Guler HP, Zapf J, Schmid C, Froesch ER. Insulin-like growth factors I and II in healthy man. Estimations of half-lives and production rates. *Acta Endocrinol (Copenh)*. 1989;121:753–8.
45. Ferry RJ Jr, Katz LE, Grimberg A, Cohen P, Weinzimer SA. Cellular actions of insulin-like growth factor binding proteins. *Horm Metab Res*. 1999;31:192–202.
46. Li R, Ferdinand JR, Loudon KW, Bowyer GS, Laidlaw S, Muyas F, et al. Mapping single-cell transcriptomes in the intra-tumoral and associated territories of kidney cancer. *Cancer Cell*. 2022;40:1583–99.e10.
47. Goveia J, Rohlenova K, Taverna F, Treps L, Conradi LC, Pircher A, et al. An integrated gene expression landscape profiling approach to identify lung tumor endothelial cell heterogeneity and angiogenic candidates. *Cancer Cell*. 2020;37:21–36.e13.
48. Ligresti G, Nagao RJ, Xue J, Choi YJ, Xu J, Ren S, et al. A novel three-dimensional human peritubular microvascular system. *J Am Soc Nephrol*. 2016;27:2370–81.
49. Pober JS, Gimbrone MA Jr, Cotran RS, Reiss CS, Burakoff SJ, Fiers W, et al. Ia expression by vascular endothelium is inducible by activated T cells and by human gamma interferon. *J Exp Med*. 1983;157:1339–53.
50. Ma W, Lehner PJ, Cresswell P, Pober JS, Johnson DR. Interferon-gamma rapidly increases peptide transporter (TAP) subunit expression and peptide transport capacity in endothelial cells. *J Biol Chem*. 1997;272:16585–90.
51. Collins T, Korman AJ, Wake CT, Boss JM, Kappes DJ, Fiers W, et al. Immune interferon activates multiple class II major histocompatibility complex genes and the associated invariant chain gene in human endothelial cells and dermal fibroblasts. *Proc Natl Acad Sci USA*. 1984;81:4917–21.
52. Chang CH, Hammer J, Loh JE, Fodor WL, Flavell RA. The activation of major histocompatibility complex class II genes by interferon regulatory factor-1 (IRF-1). *Immunogenetics*. 1992;35:378–84.
53. Ting JP, Baldwin AS. Regulation of MHC gene expression. *Curr Opin Immunol*. 1993;5:8–16.
54. Lapiere LA, Fiers W, Pober JS. Three distinct classes of regulatory cytokines control endothelial cell MHC antigen expression. Interactions with immune gamma interferon differentiate the effects of tumor necrosis factor and lymphotoxin from those of leukocyte alpha and fibroblast beta interferons. *J Exp Med*. 1988;167:794–804.
55. Nagao RJ, Marcu R, Shin YJ, Lih D, Xue J, Arang N, et al. Cyclosporine induces fenestra-associated injury in human renal microvessels in vitro. *ACS Biomater Sci Eng*. 2022;8:196–207.
56. Chevrier S, Levine JH, Zanutelli VRT, Silina K, Schulz D, Bacac M, et al. An immune atlas of clear cell renal cell carcinoma. *Cell*. 2017;169:736–49.e18.
57. Sitar T, Popowicz GM, Siwanowicz I, Huber R, Holak TA. Structural basis for the inhibition of insulin-like growth factors by insulin-like growth factor-binding proteins. *Proc Natl Acad Sci USA*. 2006;103:13028–33.
58. Dumas SJ, Meta E, Borri M, Goveia J, Rohlenova K, Concinha NV, et al. Single-cell RNA sequencing reveals renal endothelium heterogeneity and metabolic adaptation to water deprivation. *J Am Soc Nephrol*. 2020;31:118–38.
59. Hansen J, Sealon R, Menon R, Eadon MT, Lake BB, Steck B, et al. A reference tissue atlas for the human kidney. *Sci Adv*. 2022;8:eabn4965.

60. Zhang T, Niu X, Liao L, Cho EA, Yang H. The contributions of HIF-target genes to tumor growth in RCC. *PLoS One*. 2013;8:e80544.
61. Natsuizaka M, Naganuma S, Kagawa S, Ohashi S, Ahmadi A, Subramanian H, et al. Hypoxia induces IGFBP3 in esophageal squamous cancer cells through HIF-1 $\alpha$ -mediated mRNA transcription and continuous protein synthesis. *FASEB J*. 2012;26:2620–30.
62. Feldser D, Agani F, Iyer NV, Pak B, Ferreira G, Semenza GL. Reciprocal positive regulation of hypoxia-inducible factor 1 $\alpha$  and insulin-like growth factor 2. *Cancer Res*. 1999;59:3915–8.
63. Mabry RL. Topical pharmacotherapy for allergic rhinitis: new agents. *South Med J*. 1992;85:149–54.
64. Dallinga MG, Habani YI, Kayser RP, Van Noorden CJF, Klaassen I, Schlingemann RO. IGF-binding proteins 3 and 4 are regulators of sprouting angiogenesis. *Mol Biol Rep*. 2020;47:2561–72.
65. Zhao HJ, Klausen C, Zhu H, Chang HM, Li Y, Leung PCK. Bone morphogenetic protein 2 promotes human trophoblast cell invasion and endothelial-like tube formation through ID1-mediated upregulation of IGF binding protein-3. *FASEB J*. 2020;34:3151–64.
66. Lofqvist C, Chen J, Connor KM, Smith AC, Aderman CM, Liu N, et al. IGFBP3 suppresses retinopathy through suppression of oxygen-induced vessel loss and promotion of vascular regrowth. *Proc Natl Acad Sci USA*. 2007;104:10589–94.
67. Le HT, Lee HJ, Cho J, Min HY, Lee JS, Lee SJ, et al. Insulin-like growth factor binding protein-3 exerts its anti-metastatic effect in aerodigestive tract cancers by disrupting the protein stability of vimentin. *Cancers (Basel)*. 2021;13:1041.
68. Liu Y, Lv H, Li X, Liu J, Chen S, Chen Y, et al. Cyclovirobuxine inhibits the progression of clear cell renal cell carcinoma by suppressing the IGFBP3-AKT/STAT3/MAPK-Snail signalling pathway. *Int J Biol Sci*. 2021;17:3522–37.
69. Qu X, Wu Z, Dong W, Zhang T, Wang L, Pang Z, et al. Update of IGF-1 receptor inhibitor (ganitumab, dalotuzumab, cixutumumab, teprotumumab and figitumumab) effects on cancer therapy. *Oncotarget*. 2017;8:29501–18.
70. Bussolati B, Deambrosio I, Russo S, Deregibus MC, Camussi G. Altered angiogenesis and survival in human tumor-derived endothelial cells. *FASEB J*. 2003;17:1159–61.
71. Nagl L, Horvath L, Pircher A, Wolf D. Tumor endothelial cells (TECs) as potential immune directors of the tumor microenvironment - new findings and future perspectives. *Front Cell Dev Biol*. 2020;8:766.
72. Xu Y, Morales AJ, Towlerton AMH, Akilesh S, Miller CP, Tykodi SS, et al. Integrated TCR repertoire analysis and single-cell transcriptomic profiling of tumor-infiltrating T cells in renal cell carcinoma identifies shared and tumor-restricted expanded clones with unique phenotypes. *Front Oncol*. 2022;12:952252.
73. Motzer RJ, Escudier B, McDermott DF, George S, Hammers HJ, Srinivas S, et al. Nivolumab versus everolimus in advanced renal-cell carcinoma. *N Engl J Med*. 2015;373:1803–13.
74. Motzer RJ, Tannir NM, McDermott DF, Aren Frontera O, Melichar B, Choueiri TK, et al. Nivolumab plus ipilimumab versus sunitinib in advanced renal-cell carcinoma. *N Engl J Med*. 2018;378:1277–90.
75. Miller CP, Tsuchida C, Zheng Y, Himmelfarb J, Akilesh S. A 3D human renal cell carcinoma-on-a-chip for the study of tumor angiogenesis. *Neoplasia*. 2018;20:610–20.
76. Ouyang JF, Kamaraj US, Cao EY, Rackham OJL. ShinyCell: simple and sharable visualization of single-cell gene expression data. *Bioinformatics*. 2021;37:3374–6.

## ACKNOWLEDGEMENTS

We thank the generous support by philanthropic donors. We thank the patients and their families for participating in the research.

## AUTHOR CONTRIBUTIONS

S Akilesh, S S Tykodi, E H Warren, Y. Zheng, and Y Xu designed the study. Y Xu, J Xue, and S Akilesh performed the experiments. Y Xu performed the data analysis and

prepared the figures. S Akilesh, Y Xu, and S S Tykodi wrote the manuscript. All authors interpreted the data, edited the manuscript, and approved the final version. S Akilesh, S S Tykodi, and E H Warren provided funding for the study.

## FUNDING

This work was supported by a DOD Kidney Cancer Research Program Translational Research Partnership Award (KC180135 to SA and SST), a Fred Hutch/University of Washington/Seattle Children's Cancer Consortium pilot award supported by NCI P30 CA015704 to SA and the Cancer Therapeutics Endowment. This research was supported by the Shared Resources of the Fred Hutch/University of Washington Cancer Consortium (P30 CA015704) and the high-performance computing team at FHCRC funded by ORIP grant S10OD028685.

## COMPETING INTERESTS

The authors declare no competing interests.

## ETHICS APPROVAL AND CONSENT TO PARTICIPATE

This research was conducted in accordance with the guidelines of the Declaration of Helsinki and approved by the Institutional Review Board of the Fred Hutch/University of Washington Cancer Consortium (reference number: 10768). All patients provided written informed consent for donation of biological samples for research use.

## ADDITIONAL INFORMATION

**Supplementary information** The online version contains supplementary material available at <https://doi.org/10.1038/s44276-024-00047-9>.

**Correspondence** and requests for materials should be addressed to Yuexin Xu.

**Reprints and permission information** is available at <http://www.nature.com/reprints>

**Publisher's note** Springer Nature remains neutral with regard to jurisdictional claims in published maps and institutional affiliations.



**Open Access** This article is licensed under a Creative Commons Attribution 4.0 International License, which permits use, sharing, adaptation, distribution and reproduction in any medium or format, as long as you give appropriate credit to the original author(s) and the source, provide a link to the Creative Commons licence, and indicate if changes were made. The images or other third party material in this article are included in the article's Creative Commons licence, unless indicated otherwise in a credit line to the material. If material is not included in the article's Creative Commons licence and your intended use is not permitted by statutory regulation or exceeds the permitted use, you will need to obtain permission directly from the copyright holder. To view a copy of this licence, visit <http://creativecommons.org/licenses/by/4.0/>.

© The Author(s) 2024